

Article

Topology Choice and Optimization of a Bearingless Flux-Switching Motor with a Combined Winding Set

Vedran Jurdana ^{1,*}, Neven Bulic ¹ and Wolfgang Gruber ²

¹ Department of Automation and Electronics, Faculty of Engineering, University of Rijeka, Vukovarska 58, 51000 Rijeka, Croatia; nbulic@riteh.hr

² Institute of Electrical Drives and Power Electronics, Johannes Kepler University Linz, Altenberger Str. 69, 4040 Linz, Austria; wolfgang.gruber@jku.at

* Correspondence: vedran.jurdana@gmail.com; Tel.: +385-98-942-35-20

Received: 1 September 2018; Accepted: 1 November 2018; Published: 6 November 2018



Abstract: The purpose of this paper is to choose a new topology for bearingless flux-switching slice motors, regarding the number of stator and rotor poles, with a combined winding set. Additionally, the selected motor topology is optimized with finite element method (FEM) simulations to improve the performance. Bearingless slice drives feature a magnetically-suspended rotor disk passively stabilized by reluctance forces due to a permanent magnet (PM) bias flux in the air gap and actively controlled by the generation of radial bearing forces and motor torque. Usage of the combined winding set, where each phase generates both motor torque and suspension forces, opens the opportunity for a new topology. The topology choice and optimization are based on FEM simulations of several motor optimization criteria, as the passive axial, tilting and radial stiffness values and the active torque and bearing forces, which are simulated regarding the motor height and specific stator and rotor parameters. Saturation, cogging torque and cogging forces are also analyzed. The 3D FEM program ANSYS Maxwell 2015 was used. The results led to an optimized bearingless flux-switching motor topology with six new stator segments and seven rotor poles. By optimizing the geometry, a considerable improvement of performance was reached. This geometry optimization is a base for a future prototype model.

Keywords: bearingless flux-switching motor; combined winding set; finite element optimization

1. Introduction

1.1. History and Description of the Bearingless Motor

At the beginning of the 20th Century, the idea of magnetic levitation was presented, which was followed by the development of concepts to stabilize a rotor [1–5]. This research led to the development of the first bearingless motor. The bearingless motor concept started developing and spreading in universities and industry world-wide around the year 1990, especially in Japan and Switzerland [1–5]. The bearingless motor is a magnetically-levitated drive generating both torque and bearing force in one single device.

1.2. Bearingless Permanent Magnetic Flux-Switching Slice Motor

A further step of simplification in the bearingless motor setup was achieved by using a slice motor [6], which is also used in this research. “Slice” implies that the rotor is disk-shaped; hence, the length of the rotor is much smaller compared to its diameter. Thus, the axial (z-direction) and tilting directions around the x- and y-directions of this rotor can be passively stabilized in the presence of a

magnetic air-gap field [6]. In this case, stabilizing reluctance forces are created. This passive reluctance stabilization is illustrated in Figure 1.

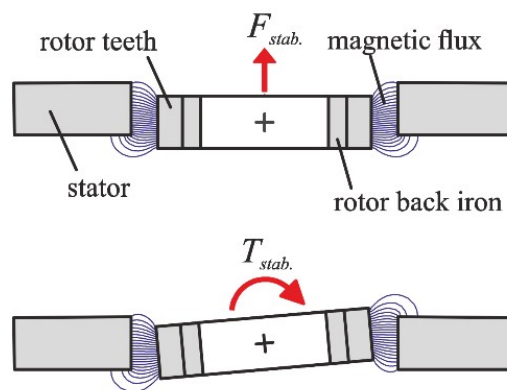


Figure 1. Passive stabilization for the axial (**top**) and tilting (**bottom**) deflection [7].

Since, with passive stabilization, three degrees of freedom are stabilized, active regulation must be provided for the radial positions (x- and y-directions) and the rotor angle [8]. This paper deals with a bearingless flux-switching slice motor. The principle of “flux-switching” is shown in Figure 2. A salient rotor is moving along stator poles, which are creating an alternating flux in the iron of the stator teeth. Each stator tooth holds a coil; subsequently, back electromotive force (EMF) is induced in the windings [9].

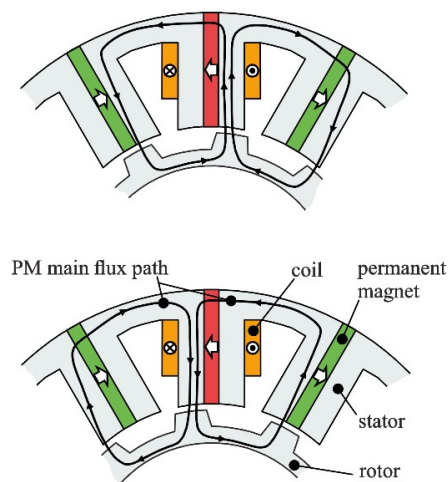


Figure 2. PM flux path depending on the rotor angle [9].

Applications of bearingless drives are pumps [10,11] in the semiconductor and medical industry, high temperature and high-speed applications and in disposable devices where the rotor has to be removed. Since the FSPM features a magnet-free rotor, rotor manufacturing costs are also lower [12,13].

1.3. New Topology with Combined Windings

Bearing force generation and torque characteristics strongly depend on the winding system. A rotating field created by a winding system featuring the same number of pole pairs as the PM field ($p_s = p_z$) generates torque and field weakening. On the other hand, a rotating stator field with a pole pair number differing by one from the PM field ($p_s \pm 1 = p_z$) generates radial bearing forces [1]. Hence, bearingless slice motors often use two different kinds of winding sets. This then is called a separated winding set, where one phase creates only motor torque, while other phases create only suspension

forces. Moreover, two connected coils are needed for one phase. In that concept, both winding sets and therefore motor torque and bearing forces are completely separated (decoupled) and can be relatively easily controlled. The disadvantages of this setup are worse efficiency and manufacturability [11]. Another possibility is to use a winding set which is called a combined winding set, which was proposed by [14]. This winding set is also used in this research. In this concept, each phase generates both motor torque and suspension forces. The advantage of this setup is the usage of one coil per phase, which is an improvement in manufacturability with reduced copper loss in the windings. Complexity is shifted to control. Nonlinear schemes and control methods have to be implemented to decouple motor torque and bearing forces properly for a bearingless motor operation [15].

The goal is to determine a new topology for operation, which uses a combined winding set. Secondly, the new topology will be optimized by FEM for improved performance. In order to simplify the understanding, the readers will first be introduced to the operating principle of the bearingless drive. Before the simulation results, geometrical parameters of the FSPM will be presented followed by the simulation explanation.

2. Setup

An existing bearingless FSPM with 12 stator segments and 10 rotor poles is shown in Figure 3 [16]. The number of stator segments is described by the parameter Q_S , while the rotor pole number is Q_R . Q_S and Q_R are changed in Section 4. However, around each stator tooth, one coil is wound. Active force and torque generation is possible through opposing coils (like 1 and 7, 2 and 8, ...) when properly energized. The main coil parameter is the magneto-motive force (MMF) of each coil. The MMF is changed from 0–1000 Aturns; 0 Aturns is used to calculate the passive stiffness, while 1000 Aturns is used to determine the active bearing force and motor torque.

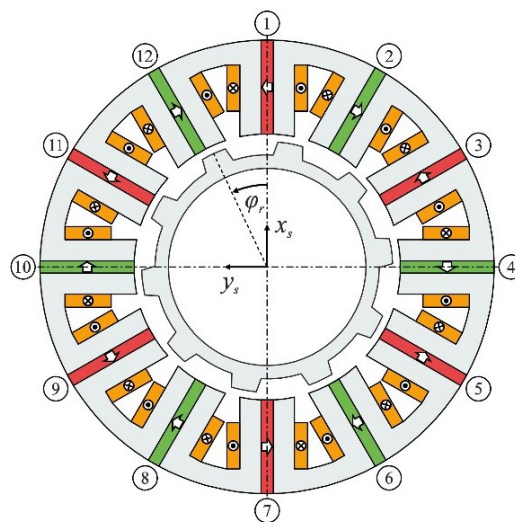


Figure 3. Cross-section of a bearingless flux-switching slice motor with twelve stator teeth and ten rotor poles [16].

2.1. Stator Teeth Geometry

The circumferential length of one stator segment is calculated by:

$$l = 2\pi \cdot \frac{d_{R0} + \delta}{Q_S}, \quad (1)$$

where the outer diameter of the rotor is given by d_{R0} and the air gap length is defined by δ .

The stator teeth are composed of two iron parts and a permanent magnet in between. Every second, the PM has the opposite polarization. The circumferential length of the iron part

of the stator tooth is defined by parameter w_{fc} . The PM's radial length is w_m , while its length is defined by the parameter l_m . The thickness of the stator segment back yoke is defined by the parameter w_{fr} and controlled by parameter $w_{ironratio2}$ by:

$$w_{fr} = w_{ironratio2} \cdot w_{fc} \tag{2}$$

These stator parameters are shown in Figure 4.

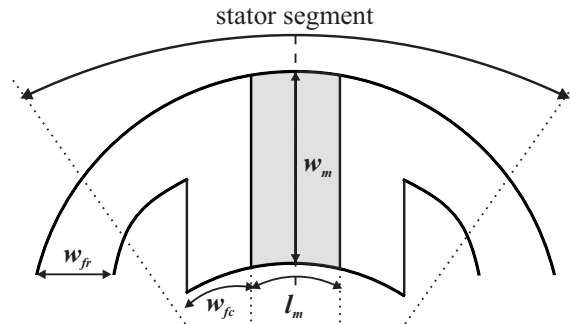


Figure 4. Cross-section of a stator segment with the corresponding parameters.

2.2. Rotor Geometry

The rotor is disk-shaped with salient poles. Apart from the outer diameter of the rotor (d_{Ro}), the inner diameter of the rotor is called d_{Ri} and calculated by:

$$w_{fr} = w_{ironratio2} \cdot w_{fc} \tag{3}$$

where t_{height} defines radial height of the rotor teeth.

Furthermore, it is important to mention the three rotor parameters that are optimized. The first one is M_r , which influences the parameter β_{Ro} , representing the outer circumferential length of the stator teeth defined as:

$$\beta_{Ro} = \frac{360 \cdot w_{fc} \cdot M_r}{d_{Ro} \cdot \pi \cdot \frac{360}{Q_R}} \tag{4}$$

The second optimization parameter is $M_{rheight}$, which changes the radial length of the rotor teeth t_{height} by:

$$t_{height} = \frac{\beta_{Ro} \cdot \pi \cdot d_{Ro} \cdot M_{rheight}}{Q_R} \tag{5}$$

The last optimization parameter is β_{Ri} , which changes the inner circumferential length of the rotor tooth along with the parameter α_r , representing the rotor pole angle. The rotor parameters are shown in Figure 5.

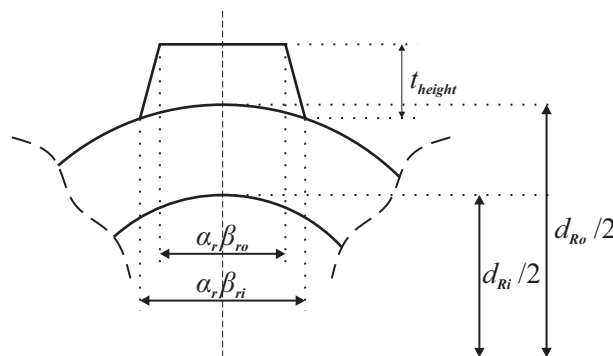


Figure 5. Cross-section of a rotor pole with corresponding parameters.

2.3. Motor Height

The motor height in the z-direction is changed by the parameter m_{height} . With the need to add or remove the stator or rotor height on constant parameter m_{height} , the two following parameters are defined: s_{height} changes the stator height, while the parameter r_{height} sets the additional rotor height.

2.4. Air Gap

Some industrial applications demand motors with an increased air gap. A larger air gap simplifies the hermetic separation of the stator and rotor, but leads to reduced overall performance [16]. With smaller air gaps, higher torque and bearing forces are generated, but the radial destabilizing forces are also increasing. In this research, the air gap length δ is set to 3 mm due to the necessity of a process chamber wall in the air gap.

2.5. Magnetic Saturation

Magnetic saturation leads to nonlinear motor behavior. Magnetic saturation is a characteristic of ferromagnetic materials where each material reaches saturation at different values. Since the force and motor torque of the FSPM are not decoupled any longer if the stator or rotor iron is magnetically saturated, magnetic flux density in FSPM should not exceed 1.5 T. In the simulations for passive stiffness without current through the coils, the risk of saturation is low, but in the simulations for active bearing forces and motor torque, it is necessary to check for iron saturation. Figure 6 shows one part of the FSPM with its magnetic flux density where different colors present the value of magnetic saturation. Red-colored parts are saturated as they feature over 1.5 T of magnetic flux density. The saturation can be avoided in two ways:

- use lower coil currents;
- change the back yoke of the stator iron (parameter w_{fr}) to increase the cross-sections of the back yoke.

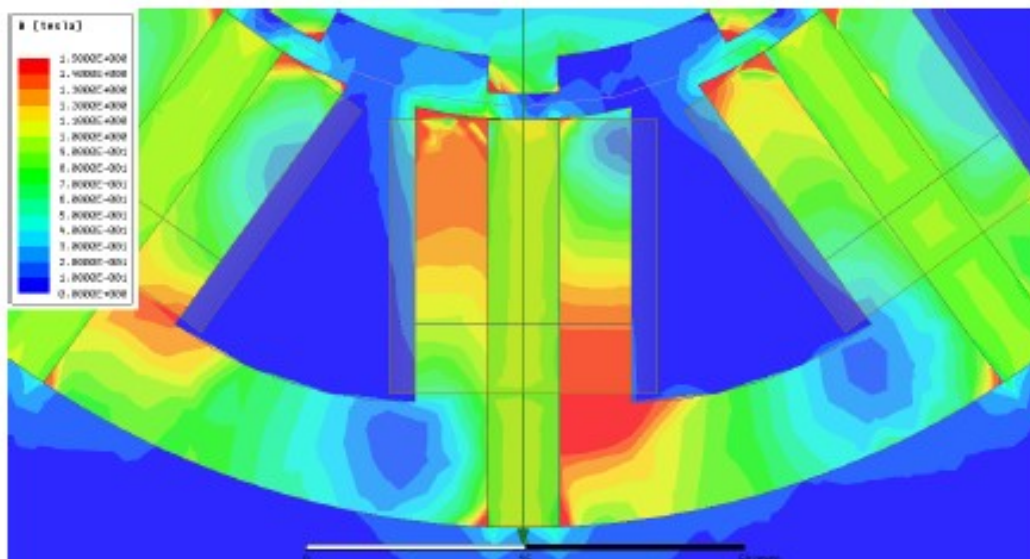


Figure 6. Part of the FSPM with its magnetic flux density.

3. Simulations

A parametric geometric model and a magnetostatic simulation setup are implemented in ANSYS Maxwell 3D FEM program. The results of the topology choice and optimization based on the simulations in this program are described in the next sections.

3.1. Simulation Parameters

In order to move or rotate the rotor in the simulations, the parameters in Table 1 are used.

Table 1. Simulation parameters.

Parameter	Description
z_move	axial deflection of the rotor (z-axis), mm
rotate_z	rotor angle, deg
x_move	radial deflection of the rotor (x-axis)
y_move	radial deflection of the rotor (y-axis)
tilting_x	rotor tilting (x-axis)
tilting_y	rotor tilting (y-axis)

3.2. Motor Optimization Criteria

The motor optimization criteria are the passive stiffness values and the active torque and force generation. The topology selection and further optimization of the chosen motor topology are based on the results of the following motor optimization criteria. It is aimed to have high motor torque and suspension forces with good passive stabilization in the axial and tilting direction [16].

3.2.1. Passive Stiffness Values

Reluctant forces are exerted on the deflected rotor due to the bias flux of the PMs in the air gap. Three degrees of freedom are stabilized by three passive forces. These passive stiffnesses are the following:

- Axial stiffness (k_z in N/mm) is defined as stabilizing force per axial deflection of the rotor in the z-direction. In the FEM simulations, the rotor is displaced 1 mm from its center position. The value of the axial stiffness is negative and thus stabilizing. Hence, it is desirable to achieve high absolute values;
- Tilting stiffness (k_{φ_x} and k_{φ_y} in Nm/deg) is defined as the stabilizing motor torque per degree due to PM reluctance forces when the rotor is tilted around the x- and y-axis. In the FEM simulations, the rotor is tilted 1 deg around the x- and y-axis, respectively, and the value of the tilting stiffness is negative, indicating stabilizing behavior. Again, higher absolute values are preferable;
- Radial stiffness (k_x and k_y in N/mm) is defined as destabilizing radial force per deflection on the rotor pulling the rotor and the stator together. Active bearing forces have to be generated in order to overcome these forces. The radial reluctance forces are different from the other described passive forces as they destabilize the system; thus, it is desired that the radial stiffness features smaller absolute values. In simulations, the rotor is radially displaced 1 mm in the x- and y-directions to compute the radial stiffness values.

3.2.2. Active Suspension Forces and Drive Torque

The radial rotor position is achieved by actively stabilized bearing forces. These forces and the motor torque are generated by the stator currents. Due to the used control scheme, bearing forces and motor torque must have a linear dependency on the current; therefore, saturation is not permissible. Additionally, no square force to current dependency should be present [16]. In the FEM simulation for active bearing forces and motor torque, a constant magneto-motive force is fed to one coil, and the rotor angle is varied. As one period of the rotor angle is dependent on the number of rotor poles, the simulated rotor angle is different for certain topologies. The active single-phase bearing forces, F_x and F_y , and the single-phase motor torque T_z feature a sinusoidal shape and are shown in Figure 7.

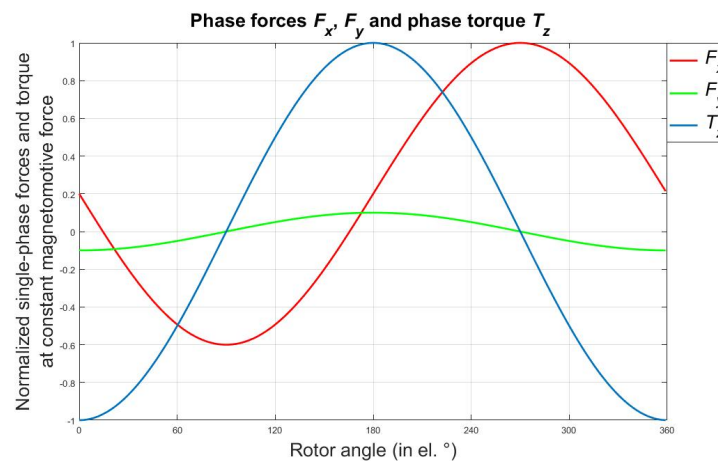


Figure 7. Part of the FSPM with its magnetic flux density.

4. Topology Choice

The first goal of this paper is to determine the most suitable topology for an FSPM. More precisely, as the “topology”, a certain number of stator segments Q_S and rotor poles Q_R are considered. The parameters Q_S and Q_R are chosen based on the simulation results regarding the motor optimization criteria. Some parameters of the FSPM are defined to be constant. These static parameters are the air gap, the axial motor height, the rotor diameter and the stator and rotor width parameters. They are summarized in Table 2 with their respective values.

Table 2. Constant parameters in the topology choice and for optimization.

Parameter	Value
δ	3 mm
m_{height}	10 mm
s_{height}	0 mm
r_{height}	0 mm
d_{Ro}	150 mm
$w_{lrratio}$	1
$w_{ironratio}$	1
$w_{pmratio}$	1
M_r	1
M_{height}	0.5
β_{Ri}	0.3

4.1. Results

The obtained FEM results are shown in Table 3, presenting the bearing forces and motor torque. The most important criteria for topology selection were:

- The cogging torque represents the torque exerted on the rotor only by the PM field ($T_{z,cogg}$ (0 At) in Table 3), which leads to torque ripples and should, hence, be small and exceeded by the active motor torque with 1000 At in one coil ($T_{z,i}$ (1000 At) in Table 3);
- The cogging forces are the forces exerted on the rotor only by the PM field ($F_{x,cogg}$ (0 At) and $F_{y,cogg}$ (0 At) in Table 3) and should be small and exceeded by the active motor active forces with 1000 At in one coil.

Table 3. Simulation results for different Q_S/Q_R topologies.

6 Stator Segments					
	4 rotor poles	5 rotor poles	6 rotor poles	7 rotor poles	8 rotor poles
$F_{x,cog}$ (0 At) (N)	0.309	4.593	0.987	2.219	0.688
$F_{y,cog}$ (0 At) (N)	0.311	3.952	0.465	0.301	0.447
$F_{x,i}$ (1000 At) (N)	11.55	18.85	22.38	17.75	9.066
$F_{y,i}$ (1000 At) (N)	8.420	7.253	5.696	1.197	4.419
$T_{z,cog}$ (0 At) (mNm)	345.322	10.429	440.84	17.617	91.61
$T_{z,i}$ (1000 At) (mNm)	264.46	287.109	410.527	378.566	292.489
8 Stator Segments					
	6 rotor poles	7 rotor poles	8 rotor poles	9 rotor poles	10 rotor poles
$F_{x,cog}$ (0 At) (N)	0.223	6.190	0.337	0.630	0.347
$F_{y,cog}$ (0 At) (N)	0.168	5.965	0.336	0.638	0.363
$F_{x,i}$ (1000 At) (N)	12.62	15.66	15.962	14.841	11.375
$F_{y,i}$ (1000 At) (N)	5.757	5.707	5.205	4.179	1.483
$T_{z,cog}$ (0 At) (mNm)	7.712	5.544	534.333	15.222	19.967
$T_{z,i}$ (1000 At) (mNm)	209.39	272.37	338.366	331.124	296.037
10 Stator Segments					
	8 rotor poles	9 rotor poles	10 rotor poles	11 rotor poles	12 rotor poles
$F_{x,cog}$ (0 At) (N)	0.269	8.716	0.346	0.512	0.228
$F_{y,cog}$ (0 At) (N)	0.272	9.037	0.291	0.493	0.196
$F_{x,i}$ (1000 At) (N)	10.99	12.515	11.884	11.854	9.964
$F_{y,i}$ (1000 At) (N)	4.638	4.983	4.536	4.099	2.838
$T_{z,cog}$ (0 At) (mNm)	44.22	13.731	623.352	6.857	23.391
$T_{z,i}$ (1000 At) (mNm)	210.273	238.515	271.287	278.891	261.102
Simulation error: ± 1					

Previous research showed that cogging torque and cogging forces depend on the magnet shapes, dimensions, locations, magnetization patterns and slot/pole combination [17]. This holds also true in this research. Additionally, axial stiffness, tilting stiffness, active forces and motor torque should be as high as possible, while the radial stiffness should be as small as possible.

4.2. Favorable Topologies

First, topologies with different parameters Q_S and Q_R are separated into feasible and unfeasible topologies in Table 4 based on the two most important rules considering the cogging forces and cogging torque described before.

Table 4. Topologies separated based on the results of Table 3.

Feasible Topologies	Unfeasible Topologies
S6R7, S8R6, S8R9, S8R10, S10R11, S10R12	S6R4, S6R5, S6R6, S6R8, S8R7, S8R8, S10R8, S10R9, S10R10

Unfeasible topologies in Table 4 feature either high cogging torque or high cogging x- and y-forces (characterized in Table 3). Hence, they become excluded from further considerations regarding the axial, radial and tilting stiffness. The topology S6R7 seems to be the most promising (Table 3); since this topology has acceptable values of cogging forces and cogging torque, its motor torque $T_{z,i}$ (1000 At) is the highest and its magnetic flux density the lower than the other simulated topologies with higher values of parameter Q_S (8 and 10).

5. Optimization

The optimization process is stepwise by changing one stator or rotor parameter after the other. Thus, the optimization is divided into four steps, which are presented in this section. The variable geometry parameters are grouped as follows:

- Motor height m_{height} , optimization of the parameters that define the motor height (in the axial z-direction), for both the stator and the rotor: s_{height} and r_{height} ;
- Stator geometry, optimization of the stator parameters: $w_{lrratio}$, $w_{ironratio}$ and $w_{pnratio}$;
- Rotor geometry, optimization of the rotor parameters: M_r , $M_{rheight}$ and β_{Ri} .

5.1. FEM Simulations and Optimization Results

Step 1: Motor height.

The first parameter that was optimized is the axial height of the stator and the rotor, which feature the same axial height at first. The values of the other parameters are given in Table 2. The simulation range and step size are presented in Table 5.

Table 5. Parameter m_{height} simulation information.

m_{height}	
Simulation range	10–20 mm
Step size	1 mm
Simulation error: ± 1	

The most important results, which are shown in Figure 8e,f, are the characteristics of the tilting stiffness values in the x- and y-direction, where higher absolute values are preferable. This leads to an increase of 14% in the x-direction and 23% in the y-direction tilting stiffness. Additionally, higher absolute values regard the axial stiffness and the active bearing forces and torque that are reached. Parameter m_{height} is set to 14 mm (instead of 10 mm).

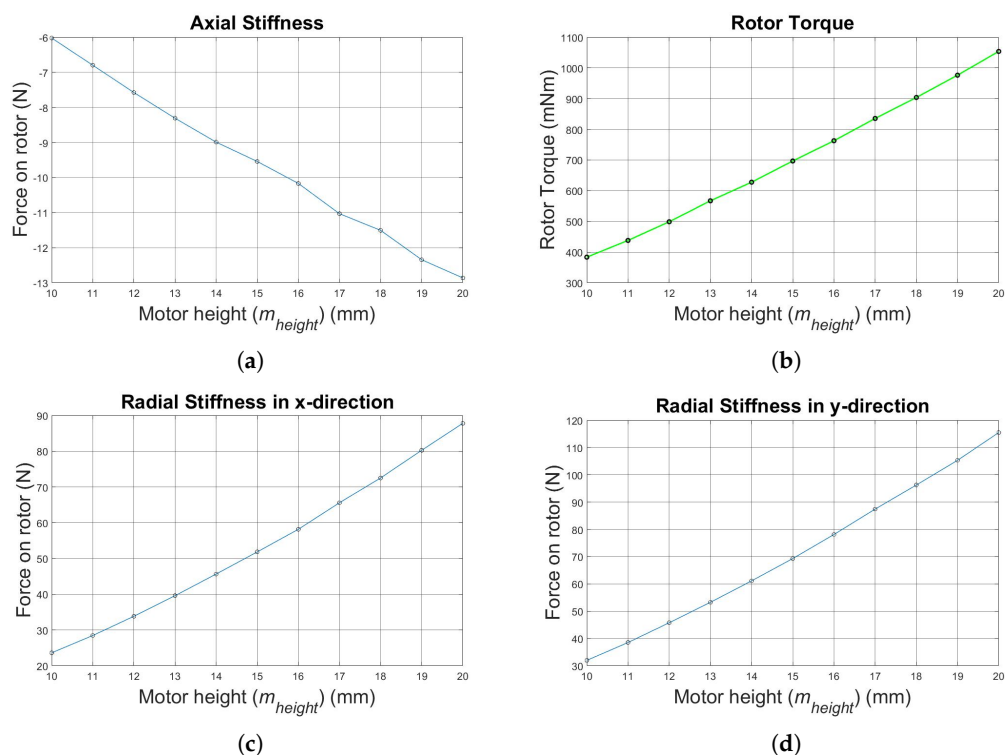


Figure 8. Cont.

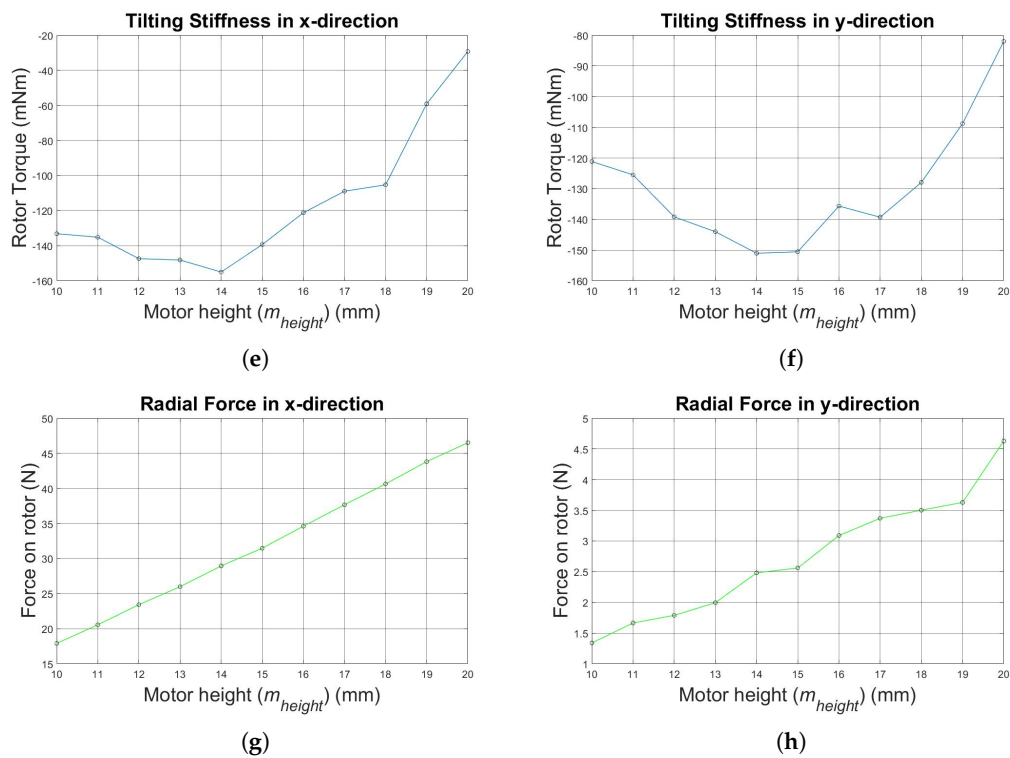


Figure 8. Simulation results for increasing motor height: (a) axial stiffness, (b) rotor torque, (c) radial stiffness in the x-direction, (d) radial stiffness in the y-direction, (e) tilting stiffness in the x-direction, (f) tilting stiffness in the y-direction, (g) radial bearing force in the x-direction and (h) radial bearing force in the y-direction.

Step 2: Stator and rotor height.

In the next step, different stator and rotor heights (in the z-direction) are reached. The reference simulations for the tilting stiffness are shown in Figure 9a for decreasing rotor height and in Figure 9b for increasing stator height.

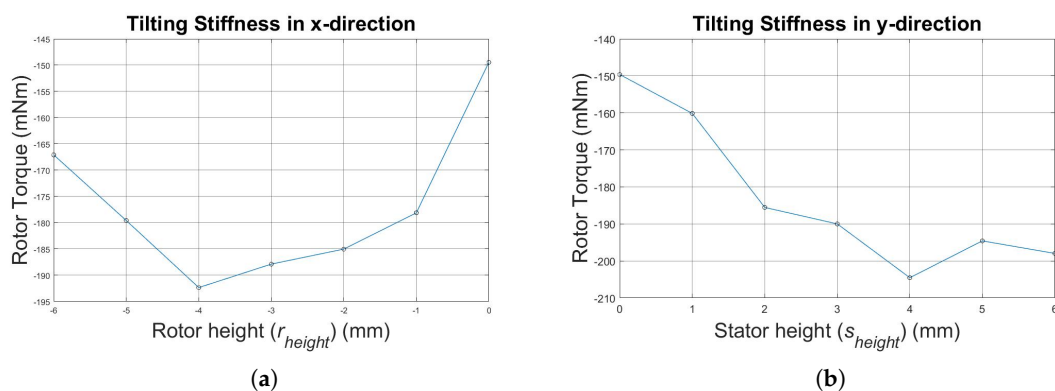


Figure 9. (a) Tilting stiffness in the x-direction with decreasing rotor height; (b) tilting stiffness in the y-direction with increasing stator height.

Since the highest absolute value for the tilting stiffness is given for a constant stator height equal to 14 mm and a decreased rotor height at 10 mm (an increase of 16%) and a constant rotor height equal to 14 mm and an increased stator height at 18 mm (an increase of 37%), further comparisons and

simulations are conducted regarding these two setups. The simulation results of those two setups are shown in Table 6. The second variant with increased stator height is selected for further consideration.

Table 6. Simulation results for decreased rotor and increased stator.

	$s_{height} = 0 \text{ mm}, r_{height} = -4 \text{ mm}$	$s_{height} = 4 \text{ mm}, r_{height} = 0 \text{ mm}$	Unit	Increase
rotor height	10	14	mm	
stator height	14	18	mm	
k_z	-7.7	-9.5	N/mm	23%
k_x	-38	-62	N/mm	61%
k_y	-50	-82	N/mm	64%
$k_{\varphi x}/k_{\varphi y}$	-180	-190	mNm/deg	5.5%
$F_{x,i}$ (1000 At)	24	35	N	45%
$F_{y,i}$ (1000 At)	2	3	N	50%
$T_{z,i}$ (1000 At)	550	800	mNm	45%
$m_{height} = 14 \text{ mm}$				
Simulation error: ± 1				

Step 3: Stator geometry.

The circumferential length of the iron part of the stator tooth (w_{fc}) is computed by parameter $w_{ironratio}$ given by:

$$w_{fc} = w_{ironratio} \cdot M, \quad (6)$$

where the parameter M is defined as the circumferential length of the stator segment divided by the sum of the stator segment parameters as defined in:

$$M = \frac{l}{w_{lrratio} + 2 \cdot w_{ironratio} + w_{pmratio}}. \quad (7)$$

The PM's length (l_m) is computed by parameter $w_{pmratio}$:

$$l_m = w_{pmratio} \cdot M. \quad (8)$$

The space between two stator teeth is set by the parameter $w_{lrratio}$. These three stator parameters $w_{lrratio}$, $w_{ironratio}$ and $w_{pmratio}$ affect the motor performance. As mentioned before, these parameters are varied one after the other. The simulation ranges and step size are given in Table 7.

Table 7. Simulation information of the stator parameters.

Parameter	Range	Step
$w_{lrratio}$	0.5–1.5	0.2
$w_{ironratio}$	Equation (9)	
$w_{pmratio}$	0.7–1.2	0.1
$m_{height} = 14 \text{ mm}, s_{height} = 4 \text{ mm}, r_{height} = 0 \text{ mm}$		
Simulation error: ± 1		

First, the parameter $w_{lrratio}$ is optimized. The characteristics for rotor torque shown in Figure 10 and tilting stiffness shown in Figure 11 are considered.

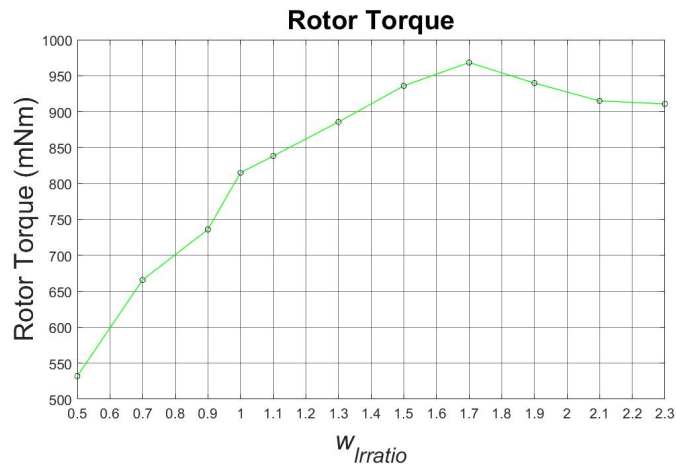


Figure 10. Rotor torque over the parameter $w_{lrratio}$.

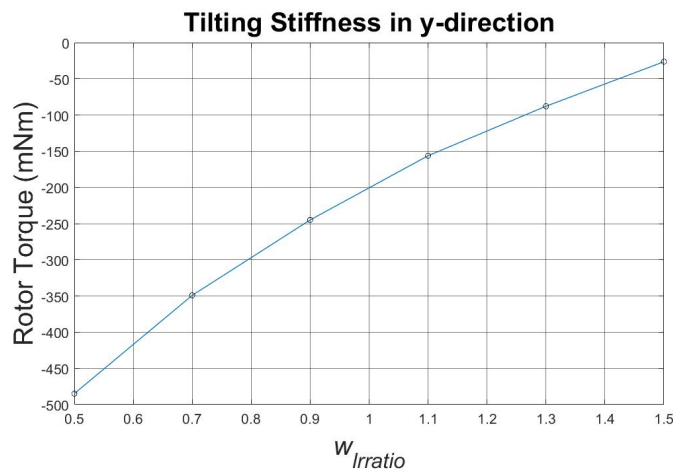


Figure 11. Tilting stiffness in the y-direction over the parameter $w_{lrratio}$.

As shown in Figure 10, the motor torque is higher for higher values of the parameter $w_{lrratio}$, while in Figure 11, the absolute tilting stiffness is higher for lower values of the parameter. Since, for both characteristics, it is better to achieve higher absolute values, a compromise of the parameter $w_{lrratio}$ had to be made, which set the parameter as one.

In a second step, simulations with different parameters $w_{ironratio}$ and $w_{pmratio}$ were conducted. Since the space between the stator teeth was previously set to one by parameter $w_{lrratio}$, to be able to simulate and see the differences in motor performance for the other two parameters $w_{ironratio}$ and $w_{pmratio}$, the motor model was redefined so that parameters $w_{ironratio}$ and $w_{lrratio}$ were no longer independent of each other. Thus, the parameter $w_{ironratio}$ is defined as follows:

$$w_{ironratio} = 1 + \frac{1 - w_{pmratio}}{2}. \quad (9)$$

Based on Table 8, the parameter $w_{pmratio}$ is defined to be 0.9. Although the motor torque and the passive stiffness do not feature their maximum, this value does not increase the cogging torque nor the cogging forces. $w_{ironratio}$ is then set to 1.05, calculated by Equation (9).

Table 8. Simulation results for different values of $w_{pmratio}$.

$w_{pmratio}$	0.7	0.8	0.9	1	1.1	1.2	Unit
k_z	−10.2	−10.8	−11.8	−12	−13	−12.8	N/mm
k_x	86.787	91.04	92.669	92.133	91.07	87.433	N/mm
k_y	88.65	91.7	95.5	100	105.8	108.1	N/mm
$k_{\varphi x}$	−170	−182	−182	−208.8	−215	−235	mNm/deg
$k_{\varphi y}$	−112	−150	−180	−205	−270	−315	mNm/deg
$F_{x,i}$ (1000 At)	38.17	38.756	40.61	40.43	40	39.087	N
$F_{y,i}$ (1000 At)	1.98	2.48	3.331	2.566	3.157	3.41	N
$T_{z,i}$ (1000 At)	781.1	815.49	849.4	890.16	890.626	880.33	mNm
$w_{lrratio} = 1$							
Simulation error: ± 1							

Step 4: Rotor geometry.

After defining all the stator parameters of the FSPM properly, the drive already showed enhanced performance. Further improvement is achieved by optimizing the rotor parameters. The simulation parameters are summarized in Table 9.

Table 9. FE simulation information of the rotor parameters.

Parameter	Range	Step
M_r	0.5–1.5	0.2
$M_{rheight}$	0.2–1	0.2
β_{Ri}	0.2–1.8	0.2
$m_{height} = 14$ mm, $s_{height} = 4$ mm, $r_{height} = 0$ mm, $w_{lrratio} = 1$, $w_{pmratio} = 0.9$, $w_{ironratio} = 1.05$		
Simulation error: ± 1		

The simulation results are shown in Tables 10–12 for the parameters M_r , $M_{rheight}$ and β_{Ri} . Apart from high torque performance, cogging torque and cogging forces had an impact in defining the rotor parameters. Due to high cogging torque and cogging forces with some values of the parameters M_r and $M_{rheight}$, these parameters could not be selected with their highest passive stiffness, active torque and force values. Thus, parameter M_r was set as 1.1 instead of 1.3, while parameter $M_{rheight}$ was set as 0.6 instead of 0.8. The cogging torque and cogging forces did not have an impact on choosing the parameter β_{Ri} . Thus, this parameter was set as 0.4 with the highest results of passive stiffness, active torque and force values. The selected parameters are shown in Tables 10–12.

Table 10. Simulation results for different values of M_r .

M_r	0.5	0.7	0.9	1.1	1.3	1.5	Unit
k_z	−9.75	−9.88	−9.6	−10.25	−11.25	−11.75	N/mm
k_x	53.7	51.8	56	70	88.8	97.3	N/mm
k_y	71	74.5	81.5	86.7	90.8	91	N/mm
$k_{\varphi x}$	−193	−187.5	−198	−194.5	−203.8	−206	mNm/deg
$k_{\varphi y}$	−163	−187.8	−194	−197	−187	−195.5	mNm/deg
$F_{x,i}$ (1000 At)	22.923	29.3685	33.503	36.5	37.20674	26.33018	N
$F_{y,i}$ (1000 At)	1.7562	2.92512	3.522144	4.0175	4.504442	4.253711	N
$T_{z,i}$ (1000 At)	464.8362	631.9887	759.4341	835.322	894.7061	865.8532	mNm
Simulation error: ± 1							

Table 11. Simulation results for different values of $M_{rheight}$.

$M_{rheight}$	0.2	0.4	0.6	0.8	1	Unit
k_z	−18.8	−10.4	−9.8	−9.5	−9.2	N/mm
k_x	74	64	62.5	61	61.8	N/mm
k_y	93	86	82.5	77.5	71.8	N/mm
$k_{\varphi x}$	−230	−203	−188.5	−190	−188	mNm/deg
$k_{\varphi y}$	−242	−208	−195	−188	−170	mNm/deg
$F_{x,i}$ (1000 At)	27.25042	34.195	35.84779	34.97191	33.84293	N
$F_{y,i}$ (1000 At)	1.60687	3.62255	4.3294	4.634218	5.47	N
$T_{z,i}$ (1000 At)	536.4645	741.24	876.3362	889.4663	889.0948	mNm
$M_r = 1.1$						
Simulation error: ± 1						

Table 12. Simulation results for different values of β_{Ri} .

β_{Ri}	0.2	0.4	0.6	0.8	Unit
$F_{x,i}$ (1000 At)	29.46025	39.79425	40.84454	40.8778	N
$F_{y,i}$ (1000 At)	8.289963	4.013222	3.328296	2.582815	N
$T_{z,i}$ (1000 At)	860.901	884.3387	865.9317	857.9403	mNm
$M_r = 1.1, M_{rheight} = 0.6$					
Simulation error: ± 1					

The main goal of the optimization was to enhance the active torque and bearing forces at the cost of radial stiffness. Additionally, increasing the stabilizing tilting stiffness in the x- and y-directions is important. The final results of the optimized FSPM motor in comparison to the unoptimized version are shown in Table 13.

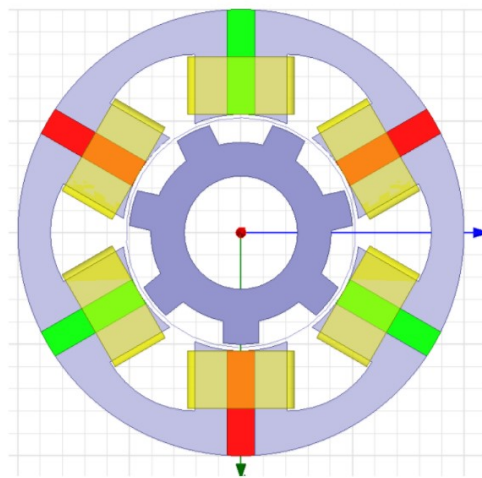
Table 13. Final results and comparison of the unoptimized and optimized FSPM motor.

	Bearingless Motor Preview before First Optimization Steps	Optimized Bearingless Motor Preview	Unit	Increase
rotor height	10	14	mm	
stator height	14	18	mm	
k_z	−7.7	−9.5	N/mm	23%
k_x	−38	−62	N/mm	61%
k_y	−50	−82	N/mm	64%
$k_{\varphi x}/k_{\varphi y}$	−180	−190	mNm/deg	5.5%
$F_{x,i}$ (1000 At)	24	35	N	45%
$F_{y,i}$ (1000 At)	2	3	N	50%
$T_{z,i}$ (1000 At)	550	800	mNm	45%
$m_{height} = 14$ mm				
Simulation error: ± 1				

Results show an increase of 52.71% in axial stiffness k_z , as well as 23.75% and 14.87% in tilting stiffness $k_{\varphi x}$ in the x-direction and $k_{\varphi y}$ in the y-direction. The radial stiffness values k_x and k_y were increased, which is unfavorable, but they were compensated with an increase of the active bearing forces $F_{x,i}$ (1000 At) and $F_{y,i}$ (1000 At). A beneficial increase of 132.02% in motor torque $T_{z,i}$ (1000 At) was achieved. Geometric parameters of the FSPM after the optimization with a comparison to the parameters before the optimization are presented in Table 14. Finally, a model of the new FSPM motor is shown in Figure 12.

Table 14. Geometric parameters of the FSPM after the optimization.

Parameter	Value before First Optimization Step	Value before First Optimization Step
m_{height}	10 mm	14 mm
s_{height}	0 mm	4 mm
r_{height}	0 mm	0 mm
$w_{lrratio}$	1	1
$w_{ironratio}$	1	1.05
$w_{pmratio}$	1	0.9
M_r	1	1.1
M_{height}	0.5	0.6
β_{Ri}	0.3	0.4

**Figure 12.** New optimized FSPM motor as illustrated in the FEM program.

6. Conclusions

In this research, the main goals are topology choice and optimization of the new FSPM model. Another possible bearingless FSPM topology is introduced. In addition to an existing FSPM prototype, with this research, a setup with only six stator teeth and seven rotor poles is considered. The new motor model is able to compensate passive stabilization and generate active torque and bearing forces. Furthermore, the geometry is optimized by simulations. The novel drive features a combined winding set, where each phase generates both motor torque and bearing force. The main advantages with this motor construction are reduced financial and construction costs by the usage of the combined winding set. A disadvantage of this research is that not all performance criteria can be satisfied. More precisely, also the unfavorable radial stiffness is increased, which is compensated with increased active radial forces. Because of cogging torque and cogging forces, some parameters had to be chosen aside from their maximum. This motor topology represents an innovation in the bearingless drive industry. Based on results of this research, a new FSPM prototype is possible.

Author Contributions: V.J. applied mathematical and computational techniques, worked with the software in designing the model and wrote the initial draft under the supervision of N.B. and W.G. who, additionally, guided with ideas and reviewed and edited the original draft. W.G. acquired funding, study materials and computing resources.

Funding: This research received no external funding.

Acknowledgments: The authors thank the Institute for Electric Drives and Power Electronics, Johannes Kepler University Linz, Austria, for enabling this work. This work has been supported by the “LCM - K2 Center for Symbiotic Mechatronics” within the framework of the Austrian COMET-K2 program.

Conflicts of Interest: The authors declare no conflict of interest.

Abbreviations

The following abbreviations are used in this manuscript:

FEM	Finite element method
PM	Permanent magnet
FSPM	Flux-switching slice motor
EMF	Electromotive force
MMF	Magneto-motive force

References

1. Bichsel, J. Beitrage Zum Lagerlosen Elektromotor. Ph.D Thesis, ETH Zurich, Zürich, Switzerland, 1990.
2. Chiba, A.; Power, D.T.; Rahman, M.A. No load characteristics of a bearingless induction motor. In Proceedings of the IEEE IAS Annual Meeting, Dearborn, MI, USA, 28 September–4 October 1991; pp. 126–132.
3. Salazar, A.O.; Chiba, A.; Fukao, T. A Review of Developments in Bearingless Motors. In Proceedings of the 7th International Symposium on Magnetic Bearings (ISMB7), Zürich, Switzerland, 23–25 August 2000.
4. Chiba, A.; Fukao, T.; Ichikawa, O.; Oshima, M.; Takemoto, M.; Dorrell, D.G. *Magnetic Bearings and Bearingless Drives*; Elsevier-News: Oxford, UK, 2005.
5. Schweitzer, G.; Maslen, E. *Magnetic Bearing Theory, Design and Application to Rotating Machinery*; Springer: Berlin/Heidelberg, Germany, 2009.
6. Schöb, R.; Barletta, N. Principle and Application of a Bearingless Slice Motor. In Proceedings of the 5th International Symposium on Magnetic Bearings (ISMB5), Kanazawa, Japan, 1996.
7. Gruber, W.; Silber, S.; Amrhein, W.; Nussbaumer, T. Design Variants of the Bearingless Segment Motor. In Proceedings of the International Symposium on Power Electronics, Electrical Drives, Automation and Motion, Pisa, Italy, 10–16 June 2010; pp. 1448–1453.
8. Karutz, P.; Nussbaumer, T.; Kolar, J.W. Magnetically levitated slice motors—An overview. In Proceedings of the Energy Conversion Congress and Exposition, San Jose, CA, USA, 20–24 September 2009; pp. 1494–1501.
9. Radman, K.; Bulić, N.; Gruber, W. Performance Evaluation of a Bearingless Flux-switching Slice Motor. In Proceedings of the Energy Conversion Congress and Exposition (ECCE), Pittsburgh, PA, USA, 14–18 September 2014.
10. Okada, Y.; Yamashiro, N.; Ohmori, K.; Masuzawa, T.; Yamane, T.; Konishi, Y.; Ueno, S. Mixed Flow Artificial Heart Pump with Axial Self-Bearing Motor. *IEEE/ASME Trans. Mech.* **2005**, *10*, 1494–1501. [[CrossRef](#)]
11. Raggl, K.; Kolar, J.W.; Nussbaumer, T. Comparison of Winding Concepts for Bearingless Pumps. In Proceedings of the 7th International Conference on Power Electronics, Daegu, Korea, 22–26 October 2007.
12. Gruber, W.; Briewasser, W.; Rothböck, M.; Schöb, R. Bearingless slice motor concepts without permanent magnet. In Proceedings of the IEEE Industrial Conference on Industrial Technology (ICIT), Cape Town, South Africa, 25–28 February 2013.
13. Gruber, W.; Bauer, W.; Radman, K. Comparison of Homopolar and Heterpolar Bearingless Reluctance Slice Motor Prototypes. *Proc. Inst. Mech. Eng. Part I J. Syst. Control Eng.* **2016**, *231*, 339–347. [[CrossRef](#)]
14. Silber, S.; Amrhein, W. Bearingless Single-Phase Motor with Concentrated Full Pitch Windings in Exterior Rotor Design. In Proceedings of the 6th International Symposium on Magnetic Bearings (ISMB6), Cambridge, MA, USA, 5–7 August 1998; pp. 476–485.
15. Grabner, H.; Amrhein, W.; Silber, S.; Gruber, W. Nonlinear Feedback Control of a Bearingless Brushless DC Motor. *IEEE/ASME Trans. Mech.* **2010**, *15*, 40–47. [[CrossRef](#)]
16. Radman, K.; Bulić, N.; Gruber, W. Geometry Optimization of a Bearingless Flux-switching Slice Motor. In Proceedings of the Electric Machines and Drives Conference (IEMDC), Coeur d’Alene, ID, USA, 10–13 May 2015.
17. Islam, M.S.; Mir, S.; Sebastian, T. Issues in reducing the Cogging Torque of Mass-Produced permanent-magnet Brushless DC Motor. *IEEE Trans. Ind. Appl.* **2004**, *40*, 813–820. [[CrossRef](#)]

